Nb-based nanoscale superconducting quantum interference devices tuned by electroannealing: Supplemental Material

Simon Collienne,[1, *] Bart Raes,[2] Wout Keijers,[2] Julian Linek,[3] Dieter Koelle,[3] Reinhold Kleiner,[3] Roman B. G. Kramer,[4] Joris Van de Vondel,[2] and Alejandro V. Silhanek[1, †]

[1] *Experimental Physics of Nanostructured Materials, Q-MAT, CESAM, Université de Liège, B-4000 Sart Tilman, Belgium*
[2] *Quantum Solid-State Physics, Department of Physics and Astronomy, KU Leuven, Celestijnenlaan 200D, B-3001 Leuven, Belgium*
[3] *Physikalisches Institut, Center for Quantum Science (CQ) and LISA+, Universität Tübingen, D-72076 Tübingen, Germany*
[4] *Université Grenoble Alpes, CNRS, Grenoble INP, Institut Néel, 38000 Grenoble, France*
(Dated: January 27, 2021)

I. *IN SITU* SCANNING ELECTRON MICROSCOPY

Fig. SM-1(a) shows the maximum resistance (R_{max}) obtained at a current I_{EA} and the minimum resistance (R_{min}) obtained after the current has been switched off for a supplementary sample. For $I_{EA} \leq 10$ mA, the increase of R_{max} with increasing I_{EA} results primarily from Joule heating, as confirmed by the fact that no change of R_{min} is observed in this current range. $I_{EA} = 10$ mA represents the threshold beyond which irreversible modifications in the constrictions are induced. For each EA step depicted in Fig. SM-1(a), we have acquired SEM images after the device has been submitted to thermal stress. A selected set of these images are shown in Fig. SM-1(b) to (e). Fig. SM-1(f) and (g) show a zoom in of the two constrictions on Fig. SM-1(e) where clear surface damage, preferentially occurring on the I- side, can be observed. One can note that no apparent structural modification are revealed for $I_{EA} \approx 10$ mA whereas clear material alteration localized at both constrictions are seen after exceeding the threshold current. The affected area is about 4200 nm^2 and 6300 nm^2 for upper and lower constrictions, respectively.

II. FINITE ELEMENT METHOD SIMULATION

Considering the non-trivial geometry of the system, the temperature inside the SQUID at low bath temperature for increasing current during the Joule heating regime has been estimated by the finite element method (FEM) based simulation software COMSOL [40]. The model assumes the 50 nm-thick Nb sample in contact with a 100 nm silicon oxide layer on top of a pure 100 x 100 x 30 μm^3 silicon wafer. The software resolves the heat transfer equation :

$$\rho_m C \frac{\partial T}{\partial t} = \kappa \nabla^2 T + Q \quad (1)$$

with ρ_m the density in kg/m^3, C the specific heat capacity in J/(kgK), T the temperature in K and κ the thermal conductivity in W/(Km). The last term in (1) is determined by the Joule heating

$$Q = \mathbf{j} \cdot \mathbf{E} = \rho \mathbf{j}^2 \quad (2)$$

with ρ the electrical resistivity in Ωm. For the stationary solution, the left hand side term of (1) vanishes. The parameters used in the simulations are summarized in Table SM-1. The thermal conductivity for Nb is taken from the bulk properties of the material. Although this value probably overestimates the real thin film value of κ [41], the increase in temperature was rather insensitive to this parameter.

	κ [W/(mK)]	ρ [$\mu\Omega$cm]	α [K^{-1}]
Nb	54	9.57	8.5×10^{-3}
SiO$_2$	1.4	10^{23}	/
Si	130	1.22×10^6	/

Table SM-1. Thermal conductivity, electrical resistivity and thermal coefficient as input parameters in COMSOL simulations.

The model includes a thermal contact at two interfaces between all three layers by forcing heat fluxes to obey:

$$q_{\perp,12} = -h(T)(T_2 - T_1) \quad (3)$$

where $q_{\perp,12}$ is the heat flux in W/m^2 from medium 1 to medium 2 and $h(T)$ the temperature-dependent heat transfer coefficient in W/(Km^2).

The main panel of Fig. SM-2 plots the evolution of the resistance as a function of current at a bath temperature $T_b = 10$ K. At low bias current, thermal dissipation is low and the temperature throughout the SQUID is homogeneous and equal to T_b. At larger currents the heat generation cannot be evacuated fast enough hence leading to an inhomogeneous temperature distribution and higher resistance. Since the temperature increases by several hundred of Kelvins during the electroannealing process, a temperature dependence of the heat transfer coefficient $h(T) = a + bT^3$ where $a = 2.99 \times 10^6$ W/(m^{2}K)

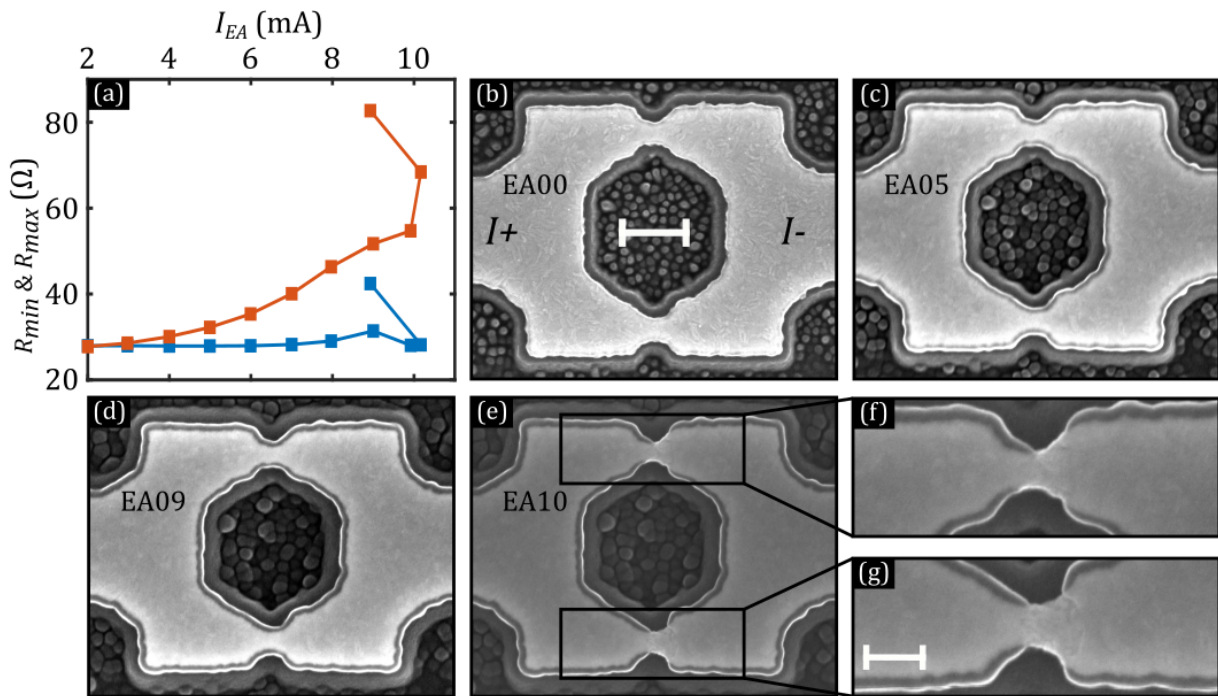* scollienne@uliege.be
† asilhanek@uliege.be

Figure SM-1. SEM images obtained during the electroannealing process for sample S2. Panel (a) shows the values of the maximum resistance (R_{max}) in red color obtained at a current I_{EA} and the minimum resistance (R_{min}) in blue color obtained after the current has been switched off. Starting from pristine state (b) EA runs produce no apparent structural modification until reaching EA10 (e). Panels (f) and (g) show a zoom-in of both Dayem bridges in panel (e). Scales bars in (b) and (g) correspond to 200 nm and 100 nm, respectively.

and $b = 12.6\ \mathrm{W/(m^2 K^4)}$ are determined in order to reproduce the experimental results. The spatial distribution of temperature, given in the inset of Fig. SM-2 for $I = 9$ mA at the end of the reversible Joule heating regime, shows a substantial rise of temperature in the entire SQUID ($\sim$ 400 K) and not only in the bridges ($\sim$ 460 K).

III. *IN SITU* ATOMIC FORCE MICROSCOPY

As can be seen in Fig. 3 of the main text, the width of the lower bridge decreases from the pristine state to panel (c). This clear tendency to shrink leads us to believe that this phenomenon may be accompanied by overgrowth perpendicularly to the plane of the SQUID. In order to reveal these features, otherwise concealed by top-view SEM images, we used *in situ* atomic force microscopy (AFM) permitting a vertical resolution of 0.1 nm. Fig. SM-3 shows a set of AFM images acquired in tapping mode at ambient conditions and for three consecutive stages of EA. As electroannealing progresses and the resistance of the device increases, a clear overgrowth develops simultaneously in both junctions achieving a height excess of 17 nm. The observed overgrowth at the constrictions could also result from the formation of Nb_2O_5 since the AFM images were acquired at atmospheric condition unlike the SEM images presented in Fig. 3 of the manuscript.
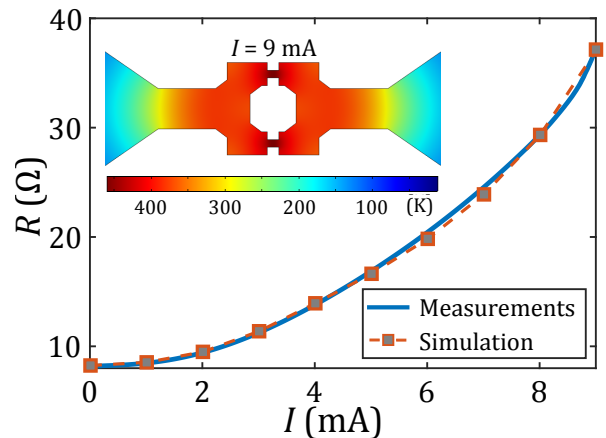

Figure SM-2. Resistance rise as a function of increasing current (sample S1) for the current range where the $R(I)$ is solely affected by Joule heating. The blue curve represents the experimental data and red squares are results from FEM simulations. The inset shows the temperature profile in the bridge for $I = 9$ mA just before EA starts.

The AFM observations were carried out in a Multimode-8 atomic force microscope at room temperature and in air with standard silicon tapping mode probe
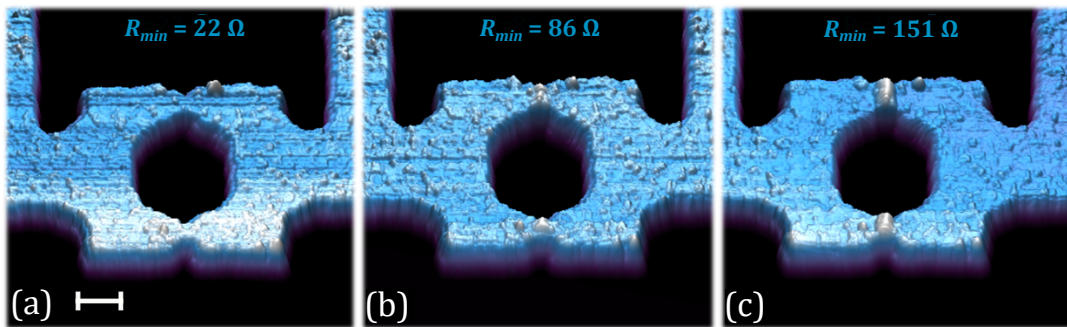
Figure SM-3. AFM images taken after three consecutive stages of electroannealing at room temperature (sample S5). The scale bar corresponds to 200 nm.

with reflex aluminium coating on the detector side of the cantilever. A 10 nm radius of curvature tip with a cantilever of 42 N/m nominal spring constant was used with a lateral scan rate of 1 Hz at 512 lines.

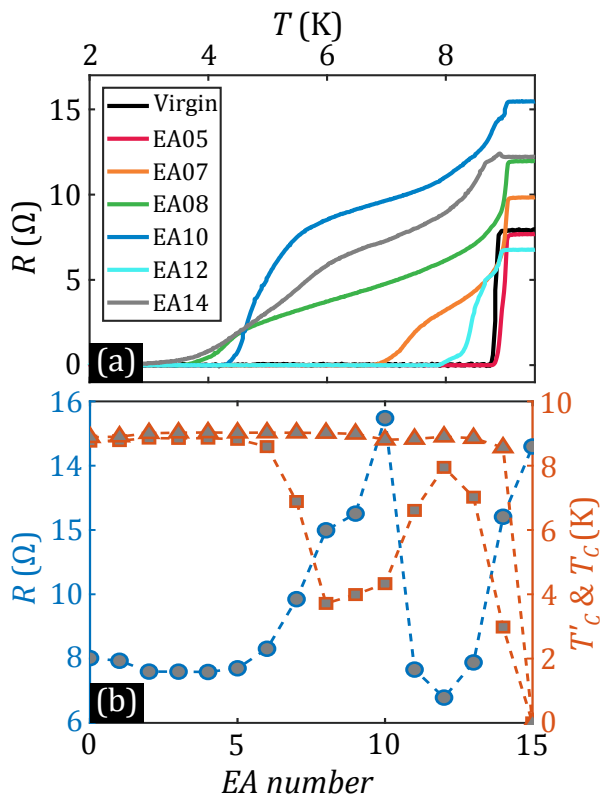## IV. WEAK LINKS SUPERCONDUCTING PROPERTIES

Figure SM-4. (a) $R(T)$ evolution for sample S4. (b) Resistance of the normal state and critical temperature taken for (a) and plotted as a function of EA number.

Fig. SM-4(a) shows a selected set of $R(T)$ curves taken after various EA steps on sample S4. The measured normal resistance and critical temperatures are summarized in Fig. SM-4(b) and present clear similarities with respect to the results shown in the main text for sample S1 (Fig. 4), demonstrating good reproducibility of the EA effects on sample behaviour.

V. COHERENCE LENGTH EVOLUTION OVER EA

Since the EA process leads to a modification of the material properties as well as the geometry of the constrictions, it is important to know if the superconducting coherence length ξ at the weak links is also affected. In order to tackle this question, we measured the superconducting-normal phase boundary $B_{c2}(T)$ after each EA step. Fig. SM-5(a) shows the $R(B)$ curves measured at $T = 1.8$ K after four EA steps. Subsequent EA steps result in a reduced B_{c2} value of the weak link characterized by a kink in the $R(B)$ curves of EA08 and EA14 as indicated by the black arrows. This kink disappears for EA11, which corresponds to an EA step at almost maximum recovery, resulting in a $R(B)$ very close to the pristine state. A set of phase boundaries is shown in Fig. SM-5(b) together with the linear fits corresponding to $B_{c2}(T) = \Phi_0/(2\pi\xi(T)^2)$ with $\xi(T) = \xi(0)/\sqrt{1 - T/T_c}$ and $\Phi_0 \approx 2.0678$ mTμm^2 is the magnetic flux quantum. Similarly as for the $R(T)$ curves, we used a criterion of $0.9R_N$ to determine B_{c2} of the SQUID arms and 0.1 Ω for estimating B_{c2} at the weak links. Note that the phase boundary first shrinks as superconductivity at the weak link is deteriorated and then recovers towards to the initial pristine state, in agreement with the data presented in Fig. SM-4. Fig. SM-5(c) summarizes the results of the fitting and shows that the superconducting coherence length at the weak links $\xi'(0)$ remains nearly unaffected by the EA process up to EA10, whereas for further EA processes, $\xi'(0)$ tends to grow.
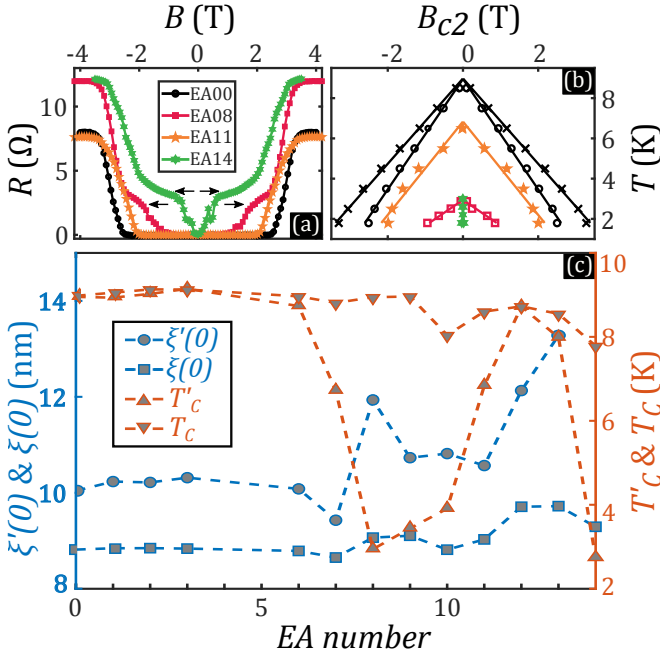
Figure SM-5. (a) Resistance vs applied magnetic field B at $T = 1.8$ K and for four different stages of EA (sample S4). EA00 corresponds to the pristine state. (b) Phase boundaries $B_{c2}(T)$ for the SQUID arms (black crosses), the constriction in the pristine state (black circles), after EA08 (red squares), EA11 (orange stars) and EA14 (green stars). In panel (c) the critical temperature T_c' and the coherence length $\xi'(0)$ of the weak links are compared with those corresponding to the SQUID arms (T_c and $\xi(0)$) after each EA step.

VI. DYNAMIC THERMAL MODEL

Recently, a time dependent thermal model for a weak link made of a superconducting constriction was proposed by Gupta *et al.* [38]. The model describes several thermal regimes mainly determined by the heat evacuation efficiency. These authors identified a dynamic regime where a non-zero voltage exists across the weak link when its temperature stabilizes between the bath temperature and the superconductor's critical temperature. The model was successfully applied to Nb based nanoSQUIDs biased at different currents [11]. In this section we implement EA processing as a way to progressively affect the thermal properties of the weak link. The thermal response of the system is ruled by a single parameter,

$$\beta(T_b) = \frac{R_N I_c^2(T_b)}{k(T_c - T_b)}, \qquad (4)$$

which quantifies the ratio between the Joule heating and the heat evacuation. In Eq.(4), R_N is the normal resistance of the two weak links in parallel, $I_c(T_b)$ is the critical current of the whole device at the bath temperature T_b and k the heat loss coefficient in W/K from the weak link through the bulk electrodes and interfaces.

Similar dimensionless parameters have been introduced in Ref.[42, 43]. For the case of a short weak link ($d \ll \xi$), and assuming a linear temperature dependence of the critical current and a temperature independent k, the β parameter is linked to the retrapping current I_r and critical current I_c as follows [38]:

$$\left[\frac{I_r}{I_c} \right]^2 = \frac{\sqrt{1 + 4\beta^4} - 1}{2\beta^2}. \qquad (5)$$

This equation allows us to determine β as a function of temperature as shown in Fig. SM-6(a). From the obtained $\beta(T_b)$ and the experimentally determined R_N, I_c and T_c, we can deduce k.

The practical application of this model requires an estimation of the value of R_N. According to Ref.[44] the retrapping current $I_r(T) = 2\sqrt{2g(T)L_0 T_c/R_N}$, with L_0 the Lorenz number, R_N the normal resistance of the two Josephson junctions in parallel and $g(T)$ a non-linear function of temperature related to the thermal conductivity in the superconducting state. Using only R_N as free fitting parameter we obtain $R_N \approx 6.2\,\Omega$. Since EA modifies R_N, a new estimation needs to be done after each EA step. In order to do so, we assume, as confirmed by SEM and AFM measurements, that all EA modifications are located at the constrictions and that the affected area does not substantially change in size. The total normal resistance is simply given by $R = R_{\text{arms}} + R_N$ where R_{arms} is the resistance of the two arms of the SQUID in parallel. Under these assumptions, we are able to estimate the resistance of the arms from the pristine state: $R_{\text{arms}} = R_{\text{pristine}} - R_N = 1.72\,\Omega$, which is assumed to remain invariant for subsequent EA processes. After each EA step, we measure R and deduce R_N as shown in the inset of Fig. SM-6(c).

To obtain an estimation of the heat loss coefficient k, we fit the experimental values of $\beta(T_b)$ with Eq.(4) using k as single fitting parameter. Fitted curves assuming a temperature-independent k are shown for EA00, EA07 and EA08 in Fig. SM-6(a), (b) and (c), respectively. For EA steps characterized by a high critical current (EA00 $\rightarrow$ EA06), the model is unable to reproduce the $\beta(T_b)$ curve with a temperature-independent k (Fig. SM-6(a)). The observed discrepancy between the theoretical model and the experimental data at low temperatures is likely due to the high value of the critical current which gives rise to substantial Joule heating for which the assumption of k being temperature-independent is no longer valid. For EA07, the dynamic thermal model is able to capture already the main features of the $\beta(T_b)$ dependence using a temperature-independent k parameter (Fig. SM-6(b)). From EA08 until EA10 the fitted curve perfectly overlaps the experimental values as can be seen for EA08 in the main panel of Fig. SM-6(c) and the obtained $k_{\text{opt}} = 11.9$ nW/K is of the same order of magnitude than the values reported by Biswas *et al.* [11] for Nb SQUIDs. After EA10, the sample becomes totally nonhysteretic and, according to Eq.(5), $\beta = 0$ for all temperatures, meaning
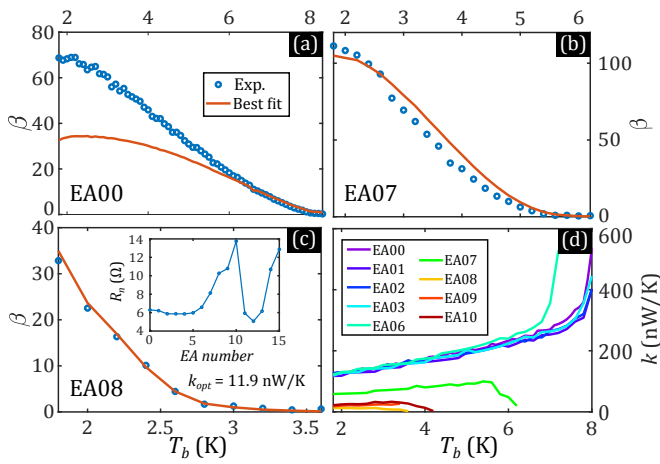
Figure SM-6. Dynamic thermal model results for sample S4. (a), (b) and (c) give experimental values of β for EA00, EA07 and EA08 respectively and the corresponding optimum k_{opt}. Inset of (c) indicates the evolution of the resistance of the two weak links in parallel under the assumption cited in the text. (d) Evolution of $k(T_b)$ for all EA steps. Note the green curve of EA07 that divide the EA steps in two distinguished thermal regimes.

that heat evacuation is always sufficient to avoid thermal runaway in the SQUID. As we will show below, the trend towards a nonhysteretic behavior is not caused by an improvement of k but rather is a consequence of the rapid decrease of I_c. Assuming that the failure of the dynamic thermal model for the initial EA steps arises from the breakdown of the temperature independence of k, we can instead calculate for each temperature and each EA steps, the value of $k(T_b)$ directly given by eq.(4) (see Fig. SM-6(d)). The observed $k(T_b)$ dependence indicates that the heat evacuation in the SQUIDs switches from a good heat evacuation regime before EA07 to a less effective one after EA07. Within these two regimes, $k(T_b)$ seems to be rather independent of the EA number. Yet, as can be seen in Sec. IV, EA07 is precisely the run where the normal resistance increases and the critical temperature decreases, indicating that the significant k reduction is owing to a structural modification in the sample.

[11] S. Biswas, C. B. Winkelmann, H. Courtois, and A. K. Gupta, "Josephson coupling in the dissipative state of a thermally hysteretic μ-SQUID," Phys. Rev. B **98** (2018).

[38] A. K. Gupta, N.l Kumar, and S. Biswas, "Temperature and phase dynamics in superconducting weak-link," J. Appl. Phys. **116**, 173901 (2014).

[40] COMSOL Multiphysics® v. 5.4. COMSOL AB, Stockholm, Sweden.

[41] A. D. Avery, S. J. Mason, D. Bassett, D. Wesenberg, and B. L. Zink, "Thermal and electrical conductivity of approximately 100-nm permalloy, Ni, Co, Al, and Cu films and examination of the Wiedemann-Franz Law,"

Phys.Rev. B **92** (2015).

[42] A. V. Gurevich and R. G. Mints, "Self-heating in normal metals and superconductors," Rev. Mod. Phys. **59**, 941-999 (1987).

[43] X. D. A. Baumans, V. S. Zharinov, E. Raymenants, S. Blanco Alvarez, J. E. Scheerder, J. Brisbois, D. Massarotti, R. Caruso, F. Tafuri, E. Janssens, V. V. Moshchalkov, J. Van de Vondel, and A. V. Silhanek, "Statistics of localized phase slips in tunable width planar point contacts," Sci. Rep. **7**, 44569 (2017).

[44] D. Hazra, J.R. Kirthley, and K. Hasselbach, "Retrapping Current in Bridge-Type Nano-SQUIDs," Phys. Rev. Appl. **4**, 024021 (2015).